

Article

Synthesis and Study of the Effect of Ba²⁺ Cations Substitution with Sr²⁺ Cations on Structural and Optical Properties of Ba_{2-x}Sr_xZnWO₆ Double Perovskite Oxides ($x = 0.00, 0.25, 0.50, 0.75, 1.00$)

Yousef A. Alsabah ^{1,2,3}, Mohamad S. AlSalhi ^{2,*}, Abdelrahman A. Elbadawi ¹ and Eltayeb M. Mustafa ¹

¹ Department of Physics, Faculty of Science and Technology, Al Neelain University, Khartoum 13314, Sudan; y.a.alsabah@gmail.com (Y.A.A.); bahlaoy.ab@gmail.com (A.A.E.); eltayebmmustafa@hotmail.com (E.M.M.)

² Research Chair in Laser Diagnosis of Cancers, Department of Physics and Astronomy, College of Science, King Saud University, Riyadh 11451, Saudi Arabia

³ Department of Physics, Faculty of Education and Applied Science, Hajjah University, Hajjah 1729, Yemen

* Correspondence: malsalhy@gmail.com; Tel: +966-14676220

Academic Editors: Yang Shao-Horn and Christian Jooss

Received: 13 February 2017; Accepted: 21 April 2017; Published: 28 April 2017

Abstract: The effect of Sr²⁺ substitution on the morphology, crystal structure, and optical properties of double perovskite oxide Ba_{2-x}Sr_xZnWO₆ ($x = 0.00, 0.25, 0.50, 0.75, 1.00$) were investigated. Scanning electronic microscopy demonstrated that all samples have similar microstructure morphology but differ in the range of grain sizes. X-ray diffraction measurements indicated that these materials crystallize in a (Fm-3m) cubic crystal structure, and also confirmed the tolerance factor. Rietveld analysis revealed that the lattice parameter decreased from 8.11834 to 8.039361 Å when the substitution of Ba²⁺ with Sr²⁺ cations increased from zero to 100%. Fourier transform infrared (FTIR) and Raman spectroscopies displayed a symmetric stretching vibration of WO₆ octahedra at 825 cm⁻¹, and an anti-symmetric stretching mode of WO₆ was observed by FTIR at 620 cm⁻¹. A strong peak at 420 cm⁻¹ was also observed in the Raman spectra and is due to the W–O–W bending vibration modes. UV-Vis diffuse reflectance spectroscopy was carried out for the series, and the band gap energy decreased from 3.27 eV for Ba₂ZnWO₆ to 3.02 and 3.06 eV for Ba_{1.75}Sr_{0.25}ZnWO₆ and Ba_{1.5}Sr_{0.5}ZnWO₆, respectively. The excitation and emission photoluminescence properties were investigated at room temperature.

Keywords: double perovskite; crystal structure; morphology; molecular structure; UV-visible; diffuse reflectance

1. Introduction

Many researchers are interested in double perovskite oxides that consist of transition metals [1]. These materials represent a large part of material science research because of the diversity in their physical and chemical characteristics, and their diverse applications [1–6], such as light harvesting (LaNiMnO₆) [2], ferroelectrics (Pb₂Mn_{0.6}Co_{0.4}WO₆) [5], Multiferroic (Bi₂NiMnO₆, Bi₂FeCrO₆) [6], superconductivity (Sr₂YRu_{0.95}Cu_{0.05}O₆) [7], magneto resistance (Sr₂FeMoO₆) [8], dielectric resonators (Ca₂AlTaO₆, SrAlTaO₆) [9], and photo-catalysis (Cs₂BiAgCl₆) [10].

A variety of devices and methods have previously been used to find and characterize new double perovskite compounds at high temperatures. Zaraq et al. [1] synthesized SrCaCoTeO₆ and SrCaNiTeO₆ compounds and used X-ray diffraction (XRD) and scanning electron microscopy (SEM) to describe their crystal structure and phase transition. Chufeng Lau et al. [2] used XRD, photoelectron spectroscopy,

and UV-Vis-NIR spectroscopy to describe the LaNiMnO_6 compound and studied the possibility for its solar cell applications. Paiva et al. [3] used the PANalytical diffractometer and Solartron 1260 impedance analyzer to study the structure and microwave properties of Sr_3WO_6 , which is used in Bluetooth and mobile system devices for microwave telecommunications through wireless antennae. By utilizing the conventional solid-state ceramic route, BiCu_2VO_6 and BiCa_2VO_6 powders, which are used in low-temperature co-fired ceramic applications, were prepared and examined using XRD, SEM, and the $\text{TE}_{01\delta}$ shielded cavity method with a network analyzer (8720ES) and temperature chamber (Delta 9023) to characterize their structure and microwave dielectric behaviors. Orlandi et al. [5] utilized the solid-state reaction route to synthesize $\text{Pb}_2\text{Mn}_{0.6}\text{Co}_{0.4}\text{WO}_6$, and used XRD with the SQUID MPMS Quantum Design magnetometer in order to investigate its crystal and magnetic structure. In addition, the perovskite compound can be used in biomedical applications. LaNiMnO_6 nanoparticles were synthesized using the co-precipitation method and were characterized by XRD using a vibration magnetometer (PPMS-9, Quantum design), Transmission electron microscopy (TEM), and UV-VIS spectroscopy to investigate the structure, magnetic, and adsorption of bovine serum albumin applications. The nanoparticles displayed good adsorption performance in the bovine serum albumin proteins. The Double-perovskite $\text{La}_2\text{NiMnO}_6$ (LNMO) nanoparticles are potential carriers for large biomolecules, which have wide use in biomedical applications.

The general chemical formula of double perovskite oxide is expressed as $\text{AA}'\text{BB}'\text{O}_6$, and the crystal structure of $\text{AA}'\text{BB}'\text{O}_6$ consists of the exchange sites of BO_6 and $\text{B}'\text{O}_6$ octahedra across the corners of the network connection. The A and A' atoms exist in the space between the BO_6 and $\text{B}'\text{O}_6$ octahedra, and can be any element from groups 1 and 2 of the periodic table, especially rare earth elements, while the B and B' cations can be any transition element [1,11].

The double-perovskite oxide compounds have a very high flexibility in crystal structure and chemical composition, where it is possible to vacinate or replace the A-sites and B-sites cations with the continuation of the octahedra network connection [1,11] such as $\text{Sr}_2\text{FeMo}_{1-x}\text{W}_x\text{O}_6$ (where $0 \leq x \leq 1$) [12], $\text{Ba}_2\text{Mg}_{1-x}\text{Ca}_x\text{WO}_6$ (where $0.0 \leq x \leq 0.15$) [13], $\text{Ca}_3\text{WO}_6:\text{Dy}^{3+}$ [14], Sr_2MWO_6 (where M = Co, Ni) [15], and $\text{Sr}_2\text{Ca}_{1-2x}\text{Eu}_x\text{Na}_x\text{MoO}_6$ [16]. In this study, we use XRD, SEM, Fourier transform infrared (FTIR) spectroscopy, photoluminescence, and UV-Vis diffuse reflectance to study the structure and optical properties of the $\text{Ba}_{2-x}\text{Sr}_x\text{ZnWO}_6$ double perovskite series ($x = 0.00, 0.25, 0.50, 0.75, 1.00$) and discuss the effect of Ba^{2+} cation substitution with Sr^{2+} cations in series behavior.

2. Results and Discussion

2.1. Structural Characterization

2.1.1. Scanning Electron Microscopy

The ESM images of the $\text{Ba}_{2-x}\text{Sr}_x\text{ZnWO}_6$ ($x = 0.00, 0.25, 0.50, 0.75, 1.00$) series are displayed in Figure 1a–e. The morphologies of all samples are identical and they appear to be highly homogeneous with no impurities. It is observed that, in all samples, the size of the particles is large and they are aggregated in groups, which is due to the higher preparation temperature. Chunfeng Lan et al. [2] observed an equivalent effect of temperature in the morphology of $\text{La}_2\text{NiMnO}_6$ double perovskite oxide. Furthermore, the images reveal the presence of fine fragments that are produced during the preparation grinding. Each of the samples has grains of various sizes, i.e., Ba_2ZnWO_6 has 1–3 μm grains, $\text{Ba}_{1.75}\text{Sr}_{0.25}\text{ZnWO}_6$ has 1–5 μm grains, $\text{Ba}_{1.5}\text{Sr}_{0.5}\text{ZnWO}_6$ has 1.5–4 μm grains, $\text{Ba}_{1.25}\text{Sr}_{0.75}\text{ZnWO}_6$ has 2–8 μm grains, and BaSrZnWO_6 has 2–7 μm grains. An Energy-dispersive X-ray spectroscopy (EDX) analysis is conducted with each sample using the SEM images. Figure 1e presents the energy dispersive X-ray spectrum from the element that formed the BaSrZnWO_6 sample. All EDX graphs confirm that all samples contain elements of the raw material preparation composition and a proportion approximating the input quantities to configure each sample with a small error, which refers to the homogeneity and crystal purity.

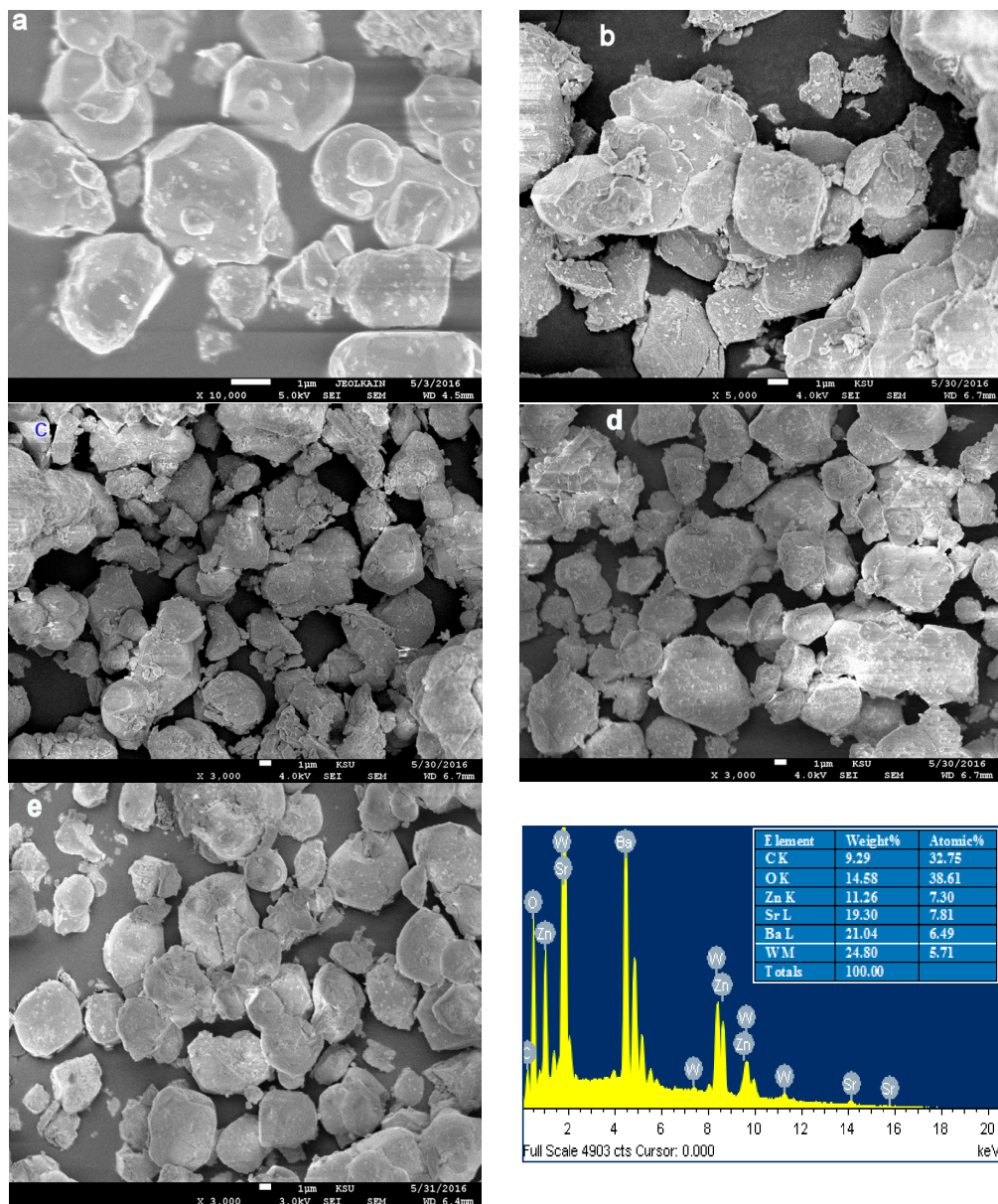


Figure 1. (a) SEM image of Ba_2ZnWO_6 ; (b) SEM image of $\text{Ba}_{1.75}\text{Sr}_{0.25}\text{ZnWO}_6$; (c) SEM image of $\text{Ba}_{1.5}\text{Sr}_{0.5}\text{ZnWO}_6$; (d) SEM image of $\text{Ba}_{1.25}\text{Sr}_{0.75}\text{ZnWO}_6$; (e) SEM image and EDX spectroscopy of BaSrZnWO_6 .

2.1.2. X-ray Powder Diffraction

The X-ray diffraction data of the perovskite oxide compounds are essential in determining the crystalline structure of the samples in terms of the Bravais lattice, atomic position, lattice parameter, and space group. Many studies refer to the importance of the study of material structure since they govern the other properties of the materials [17]. The XRD of the $\text{Ba}_{2-x}\text{Sr}_x\text{ZnWO}_6$ ($x = 0.00, 0.25, 0.50, 0.75, 1.00$) double perovskite oxide series prepared by the solid-state reaction is shown in Figure 2. The BaWO_4 and Ba_2WO_5 phases displayed as minor peaks at low intensity in the XRD pattern shown in Figure 1 are attributed to the impurities in the $\text{Ba}_{2-x}\text{Sr}_x\text{ZnWO}_6$ ($x = 0.00, 0.25, 0.50, 0.75, 1.00$) structure around 26° and 28° [18]. A plus sign and a star are used to depict them in Figure 1 when 2θ is around 26° and 28° for BaWO_4 and Ba_2WO_5 , respectively. The XRD data of each sample in the series are refined by the Rietveld method using the FullProf program. Table 1 displays the atom coordinates of all the samples obtained in the (Fm-3m) cubic crystal

structure. Figure 3 shows the XRD refinement of BaSrZnWO_6 , which is represented by a (Fm-3m) cubic structure with lattice parameters $a = b = c = 8.039361 \text{ \AA}$ and $\alpha = \beta = \gamma = 90^\circ$. Identical results are obtained for Ba_2ZnWO_6 using single-crystal X-ray and neutron diffraction [19]. Furthermore, the $\text{Ba}_{2-x}\text{Sr}_x\text{MgTeO}_6$ series was found in a (Fm-3m) cubic crystal structure [20]. The crystallite size was calculated from the Full width at half maximum (FWHMs) at the major peaks at (220) for the $\text{Ba}_{2-x}\text{Sr}_x\text{ZnWO}_6$ ($x = 0.00, 0.25, 0.50, 0.75, 1.00$) double perovskite series using the Scherer equation [21], which was observed to vary between 47.41 and 105.9 nm for the samples.

$$D = \frac{0.94 \lambda}{\beta \cos \theta'} \quad (1)$$

where D is the crystalline size, λ is the wavelength (1.5405 \AA), β is the full width at half maximum, and θ is the diffraction angle. The tolerance factor was found to be between 0.998 and 1.007, which can be calculated by

$$t = \frac{\left(1 - \left(\frac{x}{2}\right)r_A\right) + \frac{x}{2}r_A + r_o}{\sqrt{2} \left(\frac{r_B}{2} + \frac{r_B}{2} + r_o\right)} \quad (2)$$

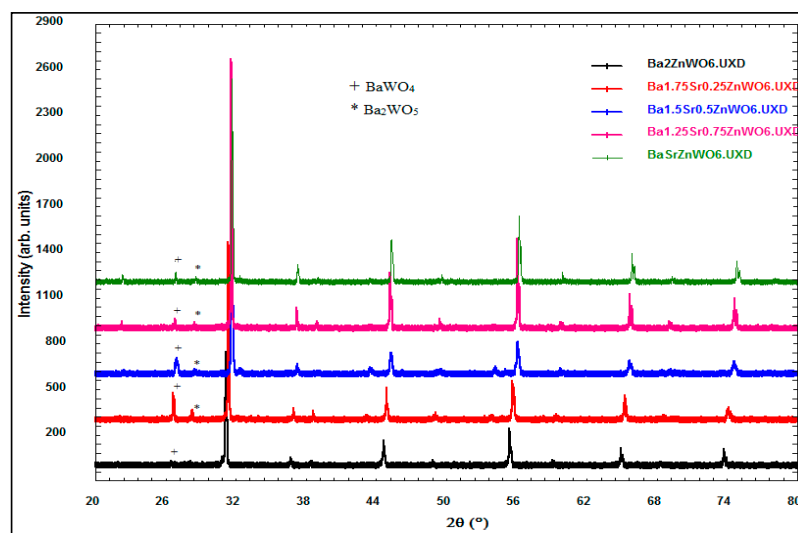


Figure 2. X-ray powder diffraction of $\text{Ba}_{2-x}\text{Sr}_x\text{ZnWO}_6$ series.

Table 1. Atom coordinates of $\text{Ba}_{2-x}\text{Sr}_x\text{ZnWO}_6$ ($x = 0.00, 0.25, 0.50, 0.75, 1.00$) double perovskite series following Rietveld refinement of X-ray powder diffraction.

Cation/Anion	Coordinates	Ba_2ZnWO_6	$\text{Ba}_{1.75}\text{Sr}_{0.25}\text{ZnWO}_6$	$\text{Ba}_{1.5}\text{Sr}_{0.5}\text{ZnWO}_6$	$\text{Ba}_{1.25}\text{Sr}_{0.75}\text{ZnWO}_6$	BaSrZnWO_6
Ba^{+2}	X	0.2500	0.2500	0.2500	0.2500	0.2500
	Y	0.2500	0.2500	0.2500	0.2500	0.2500
	Z	0.2500	0.2500	0.2500	0.2500	0.2500
Sr^{+2}	X	—	0.2500	0.2500	0.2500	0.2500
	Y	—	0.2500	0.2500	0.2500	0.2500
	Z	—	0.2500	0.2500	0.2500	0.2500
Zn^{+2}	X	0.500	0.500	0.500	0.500	0.500
	Y	0.500	0.500	0.500	0.500	0.500
	Z	0.500	0.500	0.500	0.500	0.500
W^{+6}	X	0.00	0.00	0.00	0.00	0.00
	Y	0.00	0.00	0.00	0.00	0.00
	Z	0.00	0.00	0.00	0.00	0.00
$\text{O}_1^{-2}/\text{O}_2^{-2}$	X	0.23990	0.25815	0.24414	0.22556	0.24414
	Y	0	0	0	0	0
	Z	0	0	0	0	0

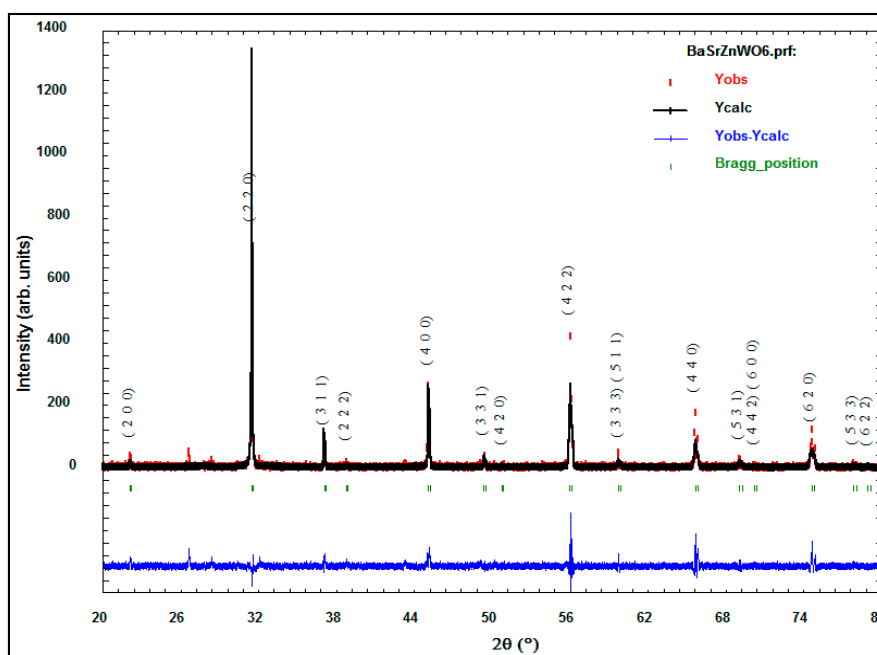


Figure 3. Refined XRD patterns of the BaSrZnWO₆.

Table 2 displays the tolerance factor and parameter of the crystal structure of Ba_{2-x}Sr_xZnWO₆ ($x = 0.00, 0.25, 0.50, 0.75, 1.00$) using the Rietveld method of refinement. The unit cell volume decreases with an increasing substitution as a result of the larger ionic radius of the Ba²⁺ cation than that of Sr²⁺.

Table 2. The tolerance factor and the parameter of crystal structure of Ba_{2-x}Sr_xZnWO₆ ($x = 0.00, 0.25, 0.50, 0.75, 1.00$) following Rietveld method refinement.

Empirical Formula	Ba ₂ ZnWO ₆	Ba _{1.75} Sr _{0.25} ZnWO ₆	Ba _{1.5} Sr _{0.5} ZnWO ₆	Ba _{1.25} Sr _{0.75} ZnWO ₆	BaSrZnWO ₆
Space group	Fm-3m	Fm-3m	Fm-3m	Fm-3m	Fm-3m
a (Å)	8.11834	8.100679	8.076869	8.060842	8.039361
$\alpha/\beta/\gamma$	90	90	90	90	90
V (Å ³)	535.0590	531.57465	526.9001	523.7707	519.5751
D (nm)	105.09	78.38	47.41	88.03	84.59
T	1.007	1.00	0.992	0.990	0.998
R_{WP}	9.78	9.71	8.87	13.6	11.3
R_p	8.75	10.2	8.15	10.3	10.8
χ^2	1.7738	1.886	1.681	2.813	2.356

2.2. Optical Studies

2.2.1. FTIR Spectroscopy

The FTIR spectra identify the crystal structure of the perovskite structure materials that have characteristic absorption bands in the 850–400 cm⁻¹ region [22]. The strong high-energy anti-symmetric stretching mode of the WO₆ octahedral displayed at 620 cm⁻¹ is due to the higher charge of the tungsten cations. The symmetric stretching vibration of the WO₆ octahedral appears as a high-intensity band at about 825 cm⁻¹. Figure 4 shows the transmittance of the Ba_{2-x}Sr_xZnWO₆ double perovskite series versus wave number, and all the samples confirm the molecular bands on the perovskite oxide structure [17].

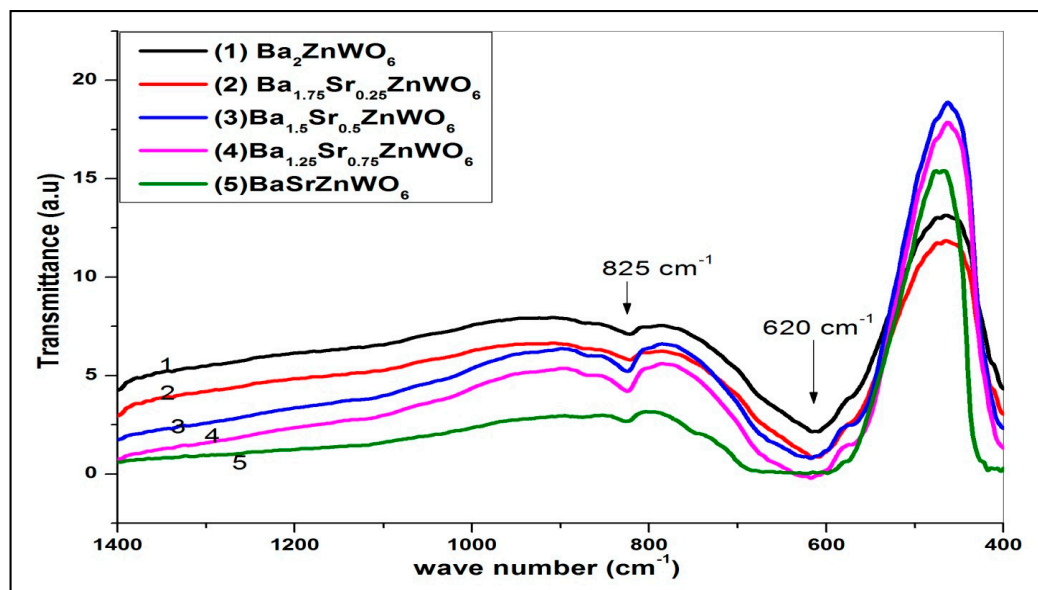


Figure 4. The Fourier transform infrared (FTIR) spectra of the $\text{Ba}_{2-x}\text{Sr}_x\text{ZnWO}_6$ double perovskite series.

2.2.2. Raman Spectroscopy

The Raman spectra of the samples are shown in Figure 5 for $\text{Ba}_{2-x}\text{Sr}_x\text{ZnWO}_6$ ($x = 0.00, 0.25, 0.50, 0.75, 1.00$). For all samples, the Raman modes are classified into two types of lattice vibration—the W–O–W bending vibration in the $200\text{--}500\text{ cm}^{-1}$ region and the W–O stretching mode between 700 and 950 cm^{-1} . This result was observed in many studies on double perovskite oxides [22,23]. Ba has a larger ionic radius (149 \AA) than that of Sr (132 \AA). When the Ba substitution increases, the effect of the Ba radius is reflected by a decrease in both the bending and stretching modes of the W–O bonds. A redshift in the Raman energy is also observed.

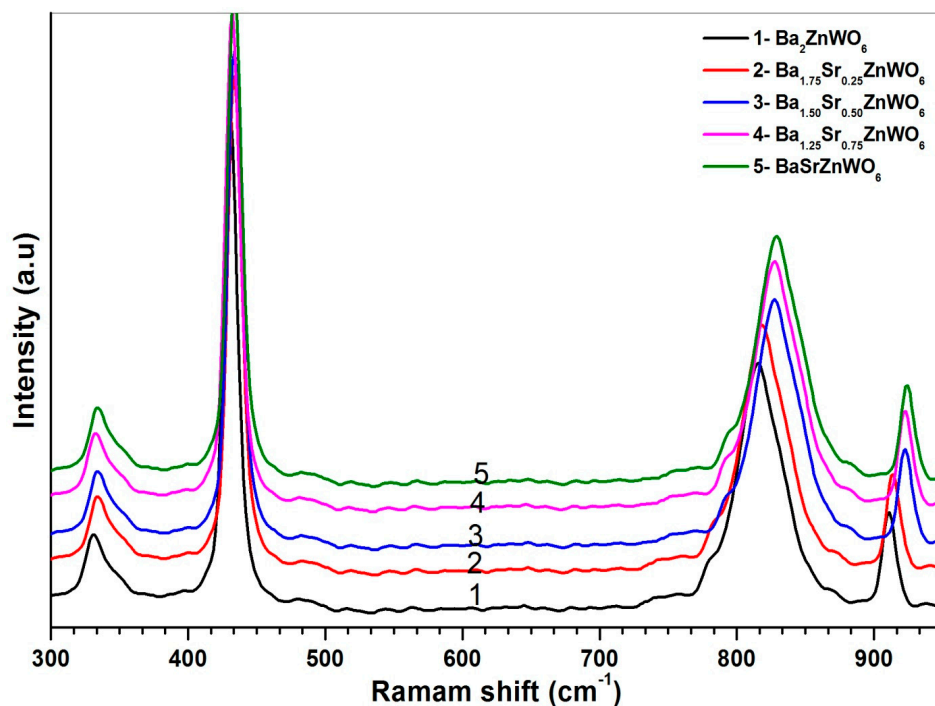


Figure 5. The Raman shift spectra of the $\text{Ba}_{2-x}\text{Sr}_x\text{ZnWO}_6$ double perovskite series.

2.2.3. UV-Visible Diffuse Reflectance Spectroscopy

Figure 6 presents the diffuse reflectance spectrum of the $\text{Ba}_{2-x}\text{Sr}_x\text{ZnWO}_6$ series at room temperature in the 200–800 nm range. The strong absorption band observed at 300–450 nm refers to the absorption edge in tungsten due to the charge transfer transition of $\text{W}^{6+} - \text{O}^{2-}$ in the lattice from the highest filled molecular orbital 2p of oxygen to the lowest empty molecular orbital 5d of tungsten [14,19,24]. The absorption band has a blue shift with an increasing substitution ratio of Ba^{2+} with Sr^{2+} cations.

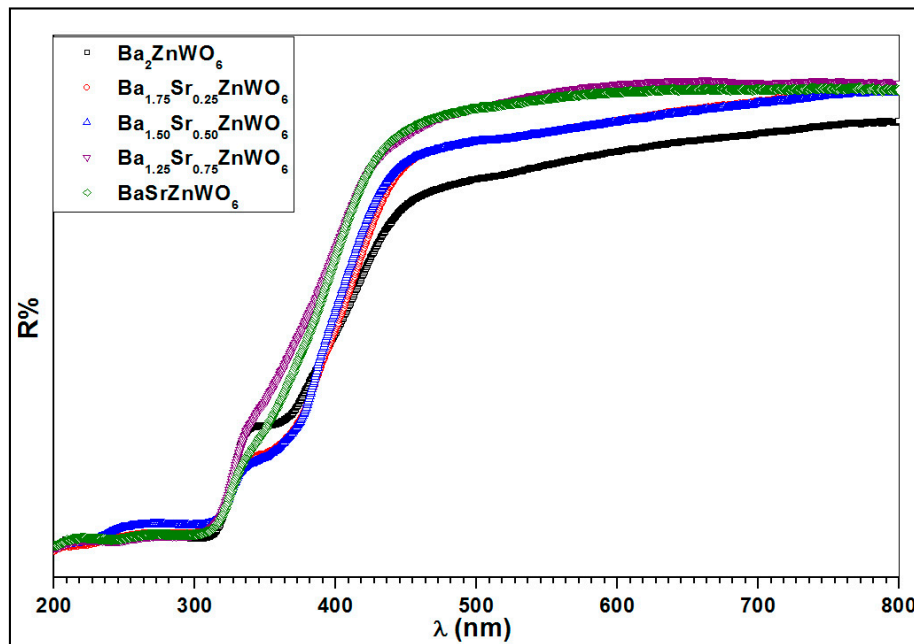


Figure 6. The diffuse reflection spectrum for $\text{Ba}_{2-x}\text{Sr}_x\text{ZnWO}_6$ ($x = 0.00, 0.25, 0.5, 0.75, \text{ and } 1.00$) double perovskite series.

The absorption coefficient can be calculated for the $\text{Ba}_{2-x}\text{Sr}_x\text{ZnWO}_6$ series from the diffuse reflectance data using the Kubelka–Munk function [25]:

$$F(R_\infty) = \frac{\alpha}{s} = \frac{(1 - R)^2}{2R} \quad (3)$$

where $F(R_\infty)$ is the KM function, α is the absorption coefficient, s is the scattering coefficient, and R is the reflection coefficient. The absorbance ($f(R)hv$) in relation to wavelength is shown in Figure 7. The absorbance can be used to observe the absorption edge for the samples that have values of 380, 410, 405, 370, and 389 nm for Ba_2ZnWO_6 , $\text{Ba}_{1.75}\text{Sr}_{0.25}\text{ZnWO}_6$, $\text{Ba}_{1.5}\text{Sr}_{0.5}\text{ZnWO}_6$, $\text{Ba}_{1.25}\text{Sr}_{0.75}\text{ZnWO}_6$, and BaSrZnWO_6 , respectively. The band gap energy of the series samples was calculated from the absorption edge [19] according to the relationship $E_g = 1240/\lambda$ (λ is the absorption edge wavelength and E_g is the band gap [26]). In addition, the band gap energy was calculated for the samples using the Tauc plot [18], as shown in Figure 8, according to Equation (4).

$$(F(R_\infty)hv)^n = A(hv - E_g) \quad (4)$$

where hv is the incident photon energy, A is a proportional constant, E_g is the band gap energy, and n takes values of 2 or 0.5 for indirect and direct transitions, respectively. Table 3 illustrates the band gap energy according to the absorption edge and Tauc plot. The results of UV–vis diffuse reflectance and the optical energy gap of the sample series indicate that they can be classified as semiconductor materials [19,27].

In the case of complete substitution of Ba²⁺ with Sr²⁺, the material of Sr₂ZnWO₆ has a monoclinic (P2₁/n) crystal structure [28,29] with 3.8 eV band gap energy [29].

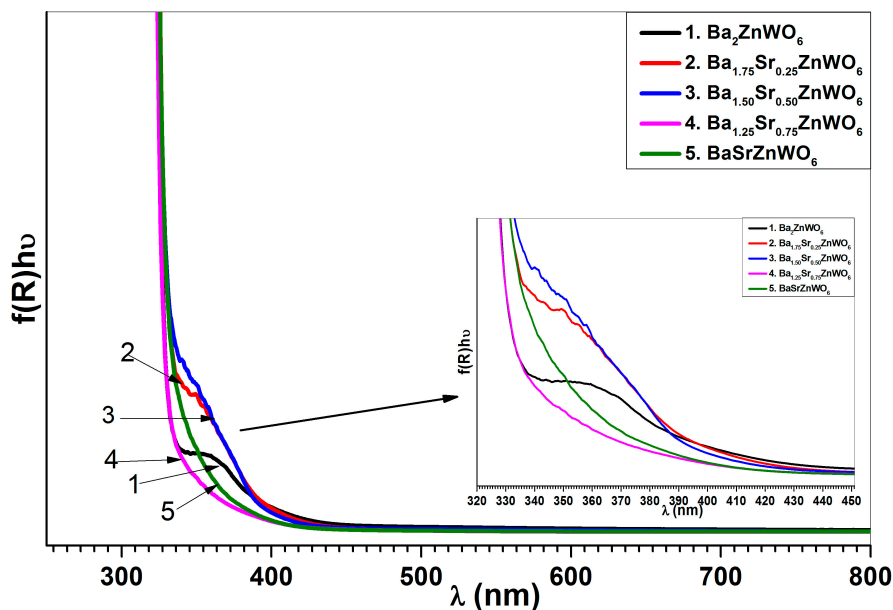


Figure 7. Absorbance versus the wavelength of Ba_{2-x}Sr_xZnWO₆ series.

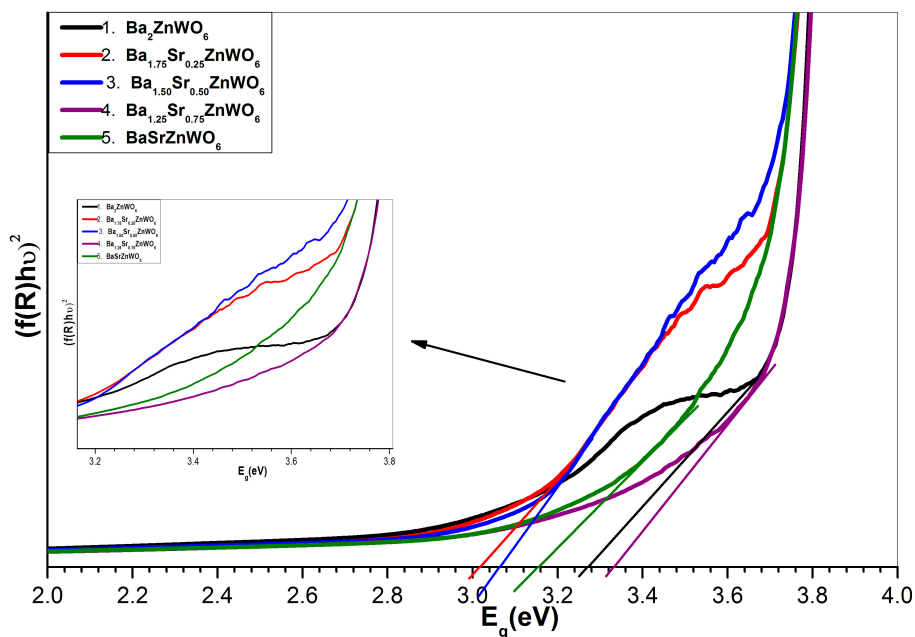


Figure 8. Indirect band gap plot for Ba_{2-x}Sr_xZnWO₆ (x = 0.00, 0.25, 0.5, 0.75, and 1.00) series.

Table 3. Illustration of band gap energy according to the absorption edge and Tauc plot for direct transition.

Bang Gap Energy	Ba ₂ ZnWO ₆	Ba _{1.75} Sr _{0.25} ZnWO ₆	Ba _{1.5} Sr _{0.5} ZnWO ₆	Ba _{1.25} Sr _{0.75} ZnWO ₆	BaSrZnWO ₆
Cut-off wavelength (nm)	380	410	405	370	389
E _g (eV) by cutoff wavelength	3.26	3.02	3.06	3.35	3.18
E _g (eV) by Tauc plot	3.27	3.02	3.07	3.34	3.16

2.2.4. Photoluminescence Spectroscopy

Figure 9 shows the excitation and photoluminescence emission spectra of the $\text{Ba}_{2-x}\text{Sr}_x\text{ZnWO}_6$ ($x = 0.00, 0.25, 0.50, 0.75, 1.00$) double perovskite oxide series. The excitation spectra shown in Figure 9a were collected when $\lambda_{em} = 380$ nm for Ba_2ZnWO_6 , $\lambda_{em} = 346$ nm for $\text{Ba}_{1.75}\text{Sr}_{0.25}\text{ZnWO}_6$, $\lambda_{em} = 344$ nm for $\text{Ba}_{1.5}\text{Sr}_{0.5}\text{ZnWO}_6$, $\lambda_{em} = 343$ nm for $\text{Ba}_{1.25}\text{Sr}_{0.75}\text{ZnWO}_6$, and $\lambda_{em} = 349$ nm for BaSrZnWO_6 . A broad band was observed between 260 and 320 nm, resulting from the electronic excitation of the O (2p) orbital-W (5d) orbital in octahedral WO_6 [14,28]. In addition, the excitation peaks of the samples decrease with the increase in the Ba^{2+} ratio substitution of Sr^{2+} cations. The photoluminescence emission of the samples was investigated at $\lambda_{ex} = 290$ nm for Ba_2ZnWO_6 , $\lambda_{ex} = 288$ nm for $\text{Ba}_{1.75}\text{Sr}_{0.25}\text{ZnWO}_6$, $\lambda_{ex} = 287$ nm for $\text{Ba}_{1.5}\text{Sr}_{0.5}\text{ZnWO}_6$, and $\lambda_{ex} = 386$ nm for $\text{Ba}_{1.25}\text{Sr}_{0.75}\text{ZnWO}_6$ and BaSrZnWO_6 displayed a spectral emission spread between 320 and 450 nm. Bugaris et al. [24] found a complimentary result where the emission peak of Ba_2ZnWO_6 displays a maximum at 539 nm when $\lambda_{ex} = 380$ nm. In addition, there is a decrease in excitation intensity peaks with an increase in substitution. The photoluminescence (PL) of Ba_2ZnWO_6 has an emission spectrum peak at 380 nm and a FWHM of 70 nm. Similarly, $\text{Ba}_{1.75}\text{Sr}_{0.25}\text{ZnWO}_6$, $\text{Ba}_{1.5}\text{Sr}_{0.5}\text{ZnWO}_6$, $\text{Ba}_{1.25}\text{Sr}_{0.75}\text{ZnWO}_6$, and BaSrZnWO_6 have peaks at 345, 344, 343, and 342 nm with FWHMs of 40, 40, 40, and 50 nm, respectively. From the peaks of photoluminescence emission, the indirect band gap energy was calculated using the $E = hc/\lambda$ equation for the series that was found to be 3.26, 3.5, 3.6, 3.6 and 3.65 eV for Ba_2ZnWO_6 , $\text{Ba}_{1.75}\text{Sr}_{0.25}\text{ZnWO}_6$, $\text{Ba}_{1.5}\text{Sr}_{0.5}\text{ZnWO}_6$, $\text{Ba}_{1.25}\text{Sr}_{0.75}\text{ZnWO}_6$, and BaSrZnWO_6 , respectively [30].

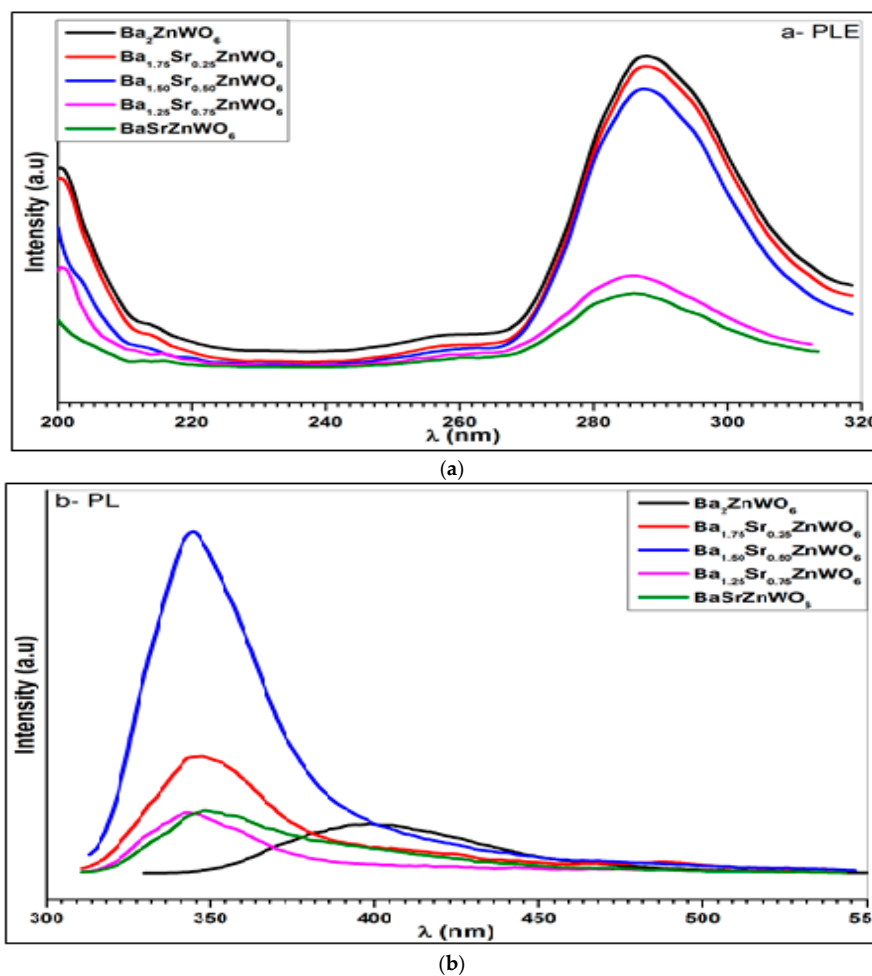
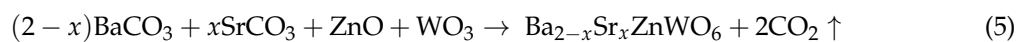


Figure 9. Photoluminescence excitation (a) and emission (b) spectrum of $\text{Ba}_{2-x}\text{Sr}_x\text{ZnWO}_6$ series.

3. Materials and Methods

3.1. Samples Preparation

$\text{Ba}_{2-x}\text{Sr}_x\text{ZnWO}_6$ (where $x = 0.00, 0.25, 0.50, 0.75, 1.00$) was synthesized using the solid-state interaction method from BaCO_3 (barium carbonite), WO_3 (tungsten trioxide), ZnO (zinc oxide), and NiO (nickel oxide) powders mixed in stoichiometric proportions according to the following chemical equation.



Initially, the materials were used as purchased from Alfa Aker with a purity of 99.99%. Several different treatments of the samples were conducted to achieve the crystal structure. The raw materials were mixed and ground in an agate mortar with acetone, kept in crucibles, and subsequently heated in air at 800 °C for 12 h twice. The sample pellets were prepared in a round shape and heated at 1000 °C twice, following which the same procedure was repeated at 1200 °C. Between the steps for the heating treatment, the sample was ground for 2 h with acetone to increase the homogeneity of the sample at a rate of 10 °C per minute during the heating and cooling process.

3.2. Sample Characterization

A Jeol JSM-6360 (JEOL Inc. Peabody, MA, USA) and high-resolution Stereo Scan LEO 440 SEM (LEO, Austin, TX, USA) were used to investigate the morphology and determine the homogeneity of the samples, as well as to obtain crystal-scale crystallization. At room temperature, the XRD data were recorded with a Bruker: D8 Advance (Bruker-Axs, Madison, WI, USA) using $\text{CuK}\alpha$ radiation ($\lambda = 1.5406 \text{ \AA}$) with a nickel filter. At 40 kV and 40 mA, data were collected for 2θ at 0.02-step sizes and 5-s count times in the 20°–80° range. The XRD data were analyzed using the Rietveld refinement method with the FullProf Suite program [31]. The crystalline size (D) [32] was calculated using the Debi–Scherer equation for all samples. At room temperature, the transmittance mode was investigated for all samples using the Satellite FTIR 5000 (ARCOptix S.A, Neuchatel, Switzerland) (with a wavelength range of 400–4000 cm^{-1}) [33], where the important bands and peaks of the perovskite structure can be assigned. Using FTIR spectroscopy collected using the KBr pellet method, the material was mixed with KBr at 1:100 ratios for the FTIR measurement in the range of 400–2000 cm^{-1} . The Raman spectra were collected in Raman HR (Stellarnet Inc., Tampa, FL, USA), using the high resolution Raman spectrometer with a range of 200–2200 cm^{-1} at 785 nm with a resolution of 4 cm^{-1} . The Raman probe attaches to the laser via FC/APC and the spectrometer via SMA 905, and has integrated Raman filters and optics with a working distance to the sample of 4.5 mm, configured for the 785 nm laser. A UV–Vis spectrophotometer (UV-2550, Shimadzu, Chiyoda-ku, Tokyo) using BaSO_4 as a reference is used to calculate the UV–Vis diffuse reflectance spectrum at room temperature. In addition, the UV–Vis reflectance spectrum is converted to absorbance using the Kubella–Munk method to estimate the edge of absorption and band gap of the $\text{Ba}_{2-x}\text{Sr}_x\text{ZnWO}_6$ double perovskite powder series. A Perkin Elmer LS55 fluorescence spectrometer (Perkin-Elmer, Wokingham, UK) was used to investigate the emission and excitation of the $\text{Ba}_{2-x}\text{Sr}_x\text{ZnWO}_6$ double perovskite series at room temperature.

4. Conclusions

The $\text{Ba}_{2-x}\text{Sr}_x\text{ZnWO}_6$ ($x = 0.00, 0.25, 0.50, 0.75, 1.00$) double perovskite series was prepared by the solid-state reaction technique. In addition, techniques such as X-ray diffraction, scanning electronic microscopy, Fourier transform infrared spectra, Raman spectra, UV-Vis diffuse reflectance, photoluminescence excitation, and emission spectra were investigated. SEM revealed that the prepared $\text{Ba}_{2-x}\text{Sr}_x\text{ZnWO}_6$ samples crystallized at micrometer scales, where the crystal structure of the samples was determined by XRD as a cubic Fm-3m space group. The lattice parameter decreased with an increase in the proportion of substitution from $x = 0$ to 1, where the result of FTIR also confirmed the

double perovskite structure. The Raman spectra of W–O bonds indicated a systematic decrease and re-shifting with an increasing Ba substitution. Strong UV-Vis absorption was found between 350 and 410 nm and smaller optical bandgap energy, 3.02 eV, was found for $\text{Ba}_{1.75}\text{Sr}_{0.25}\text{ZnWO}_6$ compared to the Sr-free sample. The excitation photoluminescence spectra displayed broad bands between 260 and 320 nm, which were assigned to the charge transfer band of $\text{Ba}_{2-x}\text{Sr}_x\text{ZnWO}_6$. $\text{Ba}_{2-x}\text{Sr}_x\text{ZnWO}_6$ displays photoluminescence in the near-UV and visible region. This feature makes $\text{Ba}_{2-x}\text{Sr}_x\text{ZnWO}_6$ a potential semiconductor in optoelectronics applications.

Acknowledgments: The authors are grateful to the Deanship of Scientific Research, King Saud University for funding through Vice Deanship of Scientific Research Chairs.

Author Contributions: Y.A.A. and M.S.A., involved designing of the work, data analysis and interpretation. A.A.E. contributed data analysis and writing of the manuscript. E.M.M. helped to improve the quality of the manuscript.

Conflicts of Interest: The authors declare no conflict of interest.

References

- Zaraq, A.; Orayech, B.; Faik, A.; Igartua, J.; Jouanneaux, A.; El Bouari, A. High temperature induced phase transitions in SrCaCoTeO_6 and SrCaNiTeO_6 ordered double perovskites. *Polyhedron* **2016**, *110*, 119–124. [[CrossRef](#)]
- Lan, C.; Zhao, S.; Xu, T.; Ma, J.; Hayase, S.; Ma, T. Investigation on structures, band gaps, and electronic structures of lead free $\text{La}_2\text{NiMnO}_6$ double perovskite materials for potential application of solar cell. *J. Alloys Compd.* **2016**, *655*, 208–214. [[CrossRef](#)]
- Paiva, D.; Silva, M.; Sombra, A.; Fechine, P. Dielectric investigation of the Sr_3WO_6 double perovskite at RF/microwave frequencies. *RSC Adv.* **2016**, *6*, 42502–42509. [[CrossRef](#)]
- Xie, H.D.; Chen, C.; Xi, H.H.; Tian, R.; Wang, X.C. Synthesis, low temperature co-firing, and microwave dielectric properties of two ceramics BiM_2VO_6 ($M = \text{Cu}, \text{Ca}$). *Ceram. Int.* **2016**, *42*, 989–995. [[CrossRef](#)]
- Orlandi, F.; Righi, L.; Mezzadri, F.; Manuel, P.; Khalyavin, D.D.; Delmonte, D.; Pernechele, C.; Cabassi, R.; Bolzoni, F.; Solzi, M.; et al. Improper Ferroelectric Contributions in the Double Perovskite $\text{Pb}_2\text{Mn}_{0.6}\text{Co}_{0.4}\text{WO}_6$ System with a Collinear Magnetic Structure. *Inorg. Chem.* **2016**, *55*, 4381–4390. [[CrossRef](#)] [[PubMed](#)]
- Shimakawa, Y.; Azuma, M.; Ichikawa, N. Multiferroic compounds with double-perovskite structures. *Materials* **2011**, *4*, 153–168. [[CrossRef](#)]
- DeMarco, M.; Blackstead, H.; Dow, J.D.; Wu, M.; Chen, D.Y.; Chen, D.F.; Haka, M.; Steve, T.; Joel, F. Magnetic phase transition in superconducting $\text{Sr}_2\text{YRu}_{0.95}\text{Cu}_{0.05}\text{O}_6$ observed by the 99 Ru Mössbauer effect. *Phys. Rev. B* **2000**, *62*, 14301–14303. [[CrossRef](#)]
- Harnagea, L.; Jurca, B.; Berthet, P. Low-field magnetoresistance up to 400 K in double perovskite $\text{Sr}_2\text{FeMoO}_6$ synthesized by a citrate route. *J. Solid State Chem.* **2014**, *211*, 219–226. [[CrossRef](#)]
- Gorodea, I.; Goanta, M.; Toma, M. Impact of A cation size of double perovskite A_2AlTaO_6 ($A = \text{Ca}, \text{Sr}, \text{Ba}$) on dielectric and catalytic properties. *J. Alloys Compd.* **2015**, *632*, 805–809. [[CrossRef](#)]
- Djerdj, I.; Popović, J.; Mal, S.; Weller, T.; Nuskol, M.; Jagličić, Z.S.; Damir, P.; Christian, S.; Pascal, V.; Roland, M.; et al. Aqueous Sol–Gel Route toward Selected Quaternary Metal Oxides with Single and Double Perovskite-Type Structure Containing Tellurium. *Cryst. Growth Des.* **2016**, *16*, 2535–2541. [[CrossRef](#)]
- Wang, Z.L.; Kang, Z.C. Perovskite and Related Structure Systems. In *Functional and Smart Materials: Functional and Smart Materials*; Springer: New York, NY, USA, 1998; Volume 3, pp. 93–149.
- Iranmanesh, M.; Lingg, M.; Stir, M.; Hulliger, J. Sol gel and ceramic synthesis of $\text{Sr}_2\text{FeMo}_{1-x}\text{W}_x\text{O}_6$ ($0 \leq x \leq 1$) double perovskites series. *RSC Adv.* **2016**, *6*, 42069–42075. [[CrossRef](#)]
- Wu, J.Y.; Bian, J.J. Structure stability and microwave dielectric properties of double perovskite ceramics $\text{Ba}_2\text{Mg}_{1-x}\text{Ca}_x\text{WO}_6$ ($0.0 \leq x \leq 0.15$). *Ceram. Int.* **2012**, *38*, 3217–3225. [[CrossRef](#)]
- Xu, D.; Yang, Z.; Sun, J.; Gao, X.; Du, J. Synthesis and luminescence properties of double-perovskite white emitting phosphor $\text{Ca}_3\text{WO}_6:\text{Dy}^{3+}$. *J. Mater. Sci. Mater. Electron.* **2016**, *27*, 8370–8377. [[CrossRef](#)]
- Tian, S.; Zhao, J.; Qiao, C.; Ji, X.; Jiang, B. Structure and properties of the ordered double perovskites Sr_2MWO_6 ($M = \text{Co}, \text{Ni}$) by sol-gel route. *Mater. Lett.* **2006**, *60*, 2747–2750. [[CrossRef](#)]

16. Xia, Z.; Sun, J.; Du, H.; Chen, D.; Sun, J. Luminescence properties of double-perovskite $\text{Sr}_2\text{Ca}_{1-2x}\text{Eu}_x\text{Na}_x\text{MoO}_6$ red-emitting phosphors prepared by the citric acid-assisted sol-gel method. *J. Mater. Sci.* **2010**, *45*, 1553–1559. [[CrossRef](#)]
17. Elbadawi, A.A.; Yassin, O.; Siddig, M.A. Effect of the Cation Size Disorder at the A-Site on the Structural Properties of SrAFeTiO_6 Double Perovskites (A = La, Pr or Nd). *J. Mater. Sci. Chem. Eng.* **2015**, *3*, 21–29.
18. Manoun, B.; Ezzahi, A.; Benmokhtar, S.; Ider, A.; Lazor, P.; Bih, L.; Igartua, J.M. X-ray diffraction and Raman spectroscopy studies of temperature and composition induced phase transitions in $\text{Ba}_{2-x}\text{Sr}_x\text{ZnWO}_6$ ($0 \leq x \leq 2$) double perovskite oxides. *J. Alloys Compd.* **2012**, *533*, 43–52. [[CrossRef](#)]
19. Bugaris, D.E.; Hodges, J.P.; Huq, A.; Zur-Loye, H.C. Crystal growth, structures, and optical properties of the cubic double perovskites Ba_2MgWO_6 and Ba_2ZnWO_6 . *J. Solid State Chem.* **2011**, *184*, 2293–2298. [[CrossRef](#)]
20. Tamraoui, Y.; Manoun, B.; Mirinioui, F.; Haloui, R.; Lazor, P. X-ray diffraction and Raman spectroscopy studies of temperature and composition induced phase transitions in $\text{Ba}_{2-x}\text{Sr}_x\text{MgTeO}_6$ ($0 \leq x \leq 2$). *J. Alloys Compd.* **2014**, *603*, 86–94. [[CrossRef](#)]
21. Mostafa, M.F.; Ata-Allah, S.S.; Youssef, A.A.A.; Refai, H.S. Electric and AC magnetic investigation of the manganites $\text{La}_{0.7}\text{Ca}_{0.3}\text{Mn}_{0.96}\text{In}_{0.04x}\text{Al}_{(1-x)0.04}\text{O}_3$; ($0.0 \leq x \leq 1.0$). *J. Magn. Magn. Mater.* **2008**, *320*, 344–353. [[CrossRef](#)]
22. Liegeois-Duyckaerts, M.; Tarte, P. Vibrational studies of molybdates, tungstates and related c compounds—III. Ordered cubic perovskites $\text{A}_2\text{B}_{\text{II}}\text{B}_{\text{VI}}\text{O}_6$. *Spectrochim. Acta Part A Mol. Spectrosc.* **1974**, *30*, 1771–1786. [[CrossRef](#)]
23. Baldinozzi, G.; Sciau, P.; Bulou, A. Raman study of the structural phase transition in the ordered perovskite Pb_2MgWO_6 . *J. Phys. Condens. Matter* **1995**, *7*, 8109. [[CrossRef](#)]
24. Xiao, N.; Shen, J.; Xiao, T.; Wu, B.; Luo, X.; Li, L.; Wang, Z.; Zhou, X. $\text{Sr}_2\text{CaW}_x\text{Mo}_{1-x}\text{O}_6:\text{Eu}^{3+}, \text{Li}^+$: An emission tunable phosphor through site symmetry and excitation wavelength. *Mater. Res. Bull.* **2015**, *70*, 684–690. [[CrossRef](#)]
25. Dutta, A.; Mukhopadhyay, P.; Sinha, T.; Shannigrahi, S.; Himanshu, A.; Sen, P.; Bandyopadhyay, S.K. $\text{Sr}_2\text{SmNbO}_6$ perovskite: Synthesis, characterization and density functional theory calculations. *Mater. Chem. Phys.* **2016**, *179*, 55–64. [[CrossRef](#)]
26. Chen, F.; Niu, C.; Yang, Q.; Li, X.; Zeng, G. Facile synthesis of visible-light-active BiOI modified Bi_2MoO_6 photocatalysts with highly enhanced photocatalytic activity. *Ceram. Int.* **2016**, *42*, 2515–2525. [[CrossRef](#)]
27. Kittel, C.; Holcomb, D.F. Introduction to solid state physics. *Am. J. Phys.* **1967**, *35*, 547–548. [[CrossRef](#)]
28. Manoun, B.; Igartua, J.M.; Lazor, P.; Ezzahi, A. High temperature induced phase transitions in Sr_2ZnWO_6 and Sr_2CoWO_6 double perovskite oxides: Raman spectroscopy as a tool. *J. Mol. Struct.* **2012**, *1029*, 81–85. [[CrossRef](#)]
29. Eng, H.W. The Crystal and Electronic Structures of Oxides Containing d0 Transition Metals in Octahedral Coordination. Ph.D. Thesis, The Ohio State University, Columbus, OH, USA, 2003.
30. Klein, P.; Nwagwu, U.; Edgar, J.H.; Freitas, J.A., Jr. Photoluminescence investigation of the indirect band gap and shallow impurities in icosahedral B_{12}As_2 . *J. Appl. Phys.* **2012**, *112*, 013508. [[CrossRef](#)]
31. Suryanarayana, C.; Norton, M.G. X-rays and Diffraction. In *X-ray Diffraction*; Springer: New York, NY, USA, 1998; Volume 1, pp. 3–19.
32. Alsabah, Y.A.; Elbadawi, A.A.; Mustafa, E.M.; Siddig, M.A. The Effect of Replacement of Zn^{2+} Cation with Ni^{2+} Cation on the Structural Properties of $\text{Ba}_2\text{Zn}_{1-x}\text{Ni}_x\text{WO}_6$ Double Perovskite Oxides ($X = 0, 0.25, 0.50, 0.75, 1$). *J. Mater. Sci. Chem. Eng.* **2016**, *4*, 61–70.
33. Kavitha, V.T.; Jose, R.; Ramakrishna, S.; Wariar, P.R.S.; Koshy, J. Combustion synthesis and characterization of $\text{Ba}_2\text{NdSbO}_6$ nanocrystals. *Bull. Mater. Sci.* **2011**, *34*, 661–665. [[CrossRef](#)]

